3D Hierarchical Boron Doped Diamond-Multilayered Graphene Nanowalls as an Efficient Supercapacitor Electrode

Debosmita Banerjee[†], Kamatchi Jothiramalingam Sankaran[‡,€], Sujit Deshmukh[†], Mateusz Ficek[§], Gourav Bhattacharya[†], Jacek Ryl[‖], Deodatta Maheshwar Phase[#], Mukul Gupta[#], Robert Bogdanowicz[§], I-Nan Lin[⊥], Aloke Kanjilal[†], Ken Haenen[*,‡,€], Susanta Sinha Roy[*,†]

[†]*Department of Physics, School of Natural Sciences, Shiv Nadar University, NH-91, Gautam Buddha Nagar, Uttar Pradesh 201314, India.*

[‡]*Institute for Materials Research (IMO), Hasselt University, 3590 Diepenbeek, Belgium.*

[€]*IMOMEC, IMEC vzw, 3590 Diepenbeek, Belgium.*

[§]*Department of Metrology and Optoelectronics, Faculty of Electronics, Telecommunications and Informatics, Gdansk University of Technology, 11/12 G. Narutowicza St., 80-233 Gdansk, Poland.*

[‖]*Department of Electrochemistry, Corrosion and Materials Engineering, Faculty of Chemistry, Gdansk University of Technology, Narutowicza 11/12, 80-233 Gdansk, Poland.*

[#]*UGC-DAE consortium for Scientific Research, Khandwa Road, Indore Madhya Pradesh 452001, India.*

[⊥]*Department of Physics, Tamkang University, Tamsui, 251 Taiwan, Republic of China.*

ABSTRACT

Synthesis of stable hybrid carbon nanostructure for high performance supercapacitor electrode with long life-cycle for electronic and energy storage devices is a real challenge. Here, we present a one-step synthesis method to produce conductive boron-doped hybrid carbon nanowalls (HCNWs), where sp^2-bonded graphene has been integrated with and over a three-dimensional curved wall-like network of sp^3-bonded diamond. The spectroscopic studies such as X-ray absorption, Raman, and X-ray photoelectrons clearly reveal the co-existence of diamond and graphene in these nanowalls, while the detailed transmission electron microscopy studies confirm the unique microstructure where a diamond nanowall is encased by a multi-layered graphene. Interestingly, these HCNWs yield a high double layer capacitance value of 0.43 mF cm^{-2} and electrode retention of 98% over 10000 cycles of charging/discharging in 1M Na$_2$SO$_4$ electrolyte. The remarkable supercapacitive performance can be attributed to the 3D interconnected network of diamond nanowalls surrounded by highly conducting graphene.

Electronic mail: susanta.roy@snu.edu.in

ken.haenen@uhasselt.be

INTRODUCTION

The increasing demand for portable electronic devices highlight the need for high performance compact energy storage equipment. Batteries and/or electrochemical supercapacitors (ESCs) are known to be the most practical, efficient and promising energy storage devices so far, though the performance of batteries are restricted by electrochemical (EC) volumetric reaction and the rate of solid-state diffusion. Also the lifetime of the best batteries (lithium ion) is limited to only hundreds or thousands of cycles.[1-2] However, in supercapacitors the charge-discharge rate is high enough to provide lifetimes over millions of cycles.[3] As a consequence, ESCs can sometimes replace batteries in applications like handheld electronics, transportation, and storage of renewable energy for the power grid, where high power delivery with long cycle life is required.[4] A large variety of active material such as graphene,[5-8] carbon nanotubes (CNTs),[9-10] activated carbon,[11-12] polymers,[13-14] and many pseudocapacitive materials[15-16] have been used as a ESC. Among them, graphene and CNTs are the most potential candidates in today's energy-storage landscape. However, their application is hindered by their low energy density values[17] and high production cost. Alternative ways to deliver a high capacitance value is to use pseudocapacitive materials i.e. oxide-based electrodes or their composites. But the limitations in their redox kinetics reactions reduce the power capabilities of pseudocapacitive ESC devices.[18-21] Therefore, designing an efficient energy storage material which can deliver high energy with a lifetime that can exceed or matches that of conventional batteries remains a challenge.

For ESC applications, especially in electrical double layer capacitor (EDLC), sp^2-bonded carbon allotropes such as graphene, CNTs, etc. have dominated over other materials due to their large specific capacitance values.[22] However, the small EC potential window (1.23 V) in aqueous solution limits their energy storage performance significantly.[23-24] On the other hand, conductive diamond electrodes (*p*- and *n*-type doped) show a comparatively larger potential

3

window in both aqueous (~3.2 V) and organic electrolytes (~4.6 V).[25-28] Also it has been speculated that diamond samples with a high defect density, show rich surface chemistry providing indeed advantages to diamond electrodes for designing new types of supercapacitors.[28-29] However, bulk boron doped diamond electrodes exhibit low EDLC values and a large interfacial impedance which hinders their performance with respect to other electrode materials.[30-31] These limitations can be solved partially by preparing nanostructured diamond material.[32-33] Moreover, integration of multiple carbon allotropes especially the combination of sp^2 and sp^3 phases (graphene-diamond, CNT-diamond etc.) in a single hybrid nanostructure has garnered attention because of their synergistic physical and electronic behaviours. Like for a graphene-diamond composite, in addition to the hardness and chemical stability of diamond, graphene offers high mobility of charge carriers, huge surface area, exceptional electrical and thermal conductivity, high aspect ratio etc. The composition (ratio of sp^3 to sp^2), morphology, microstructure and the boundary effect of the hybrid structure modify the electrochemical accessibility of the electrolyte and hence the charge transfer kinetics at the surface.[25,34] Thus, a hybrid nanostructure synthesized by a combination of two allotropes are believed to be very much promising for superior supercapacitive characteristics.

In this work, three-dimensional (3D) hierarchical carbon nanowalls (HCNWs) comprised of a boron doped diamond-multilayered graphene were synthesized in a one-step microwave plasma enhanced chemical vapour deposition (MWPECVD) technique. The supercapacitors designed from these HCNW electrodes provide a high specific capacitance value with a remarkable long-term stability. To understand the key factors responsible for their impressive energy storage performance, the HCNW electrodes were characterized in detail by different microscopic and spectroscopic tools. Furthermore, the possible mechanism for the high ESC performance of HCNWs is discussed in detail using an in-depth electrochemical characterization.

EXPERIMENTAL SECTION

HCNWs were synthesized on (100)-oriented silicon substrates using a MWPECVD (SEKI Technotron AX5400S, Japan) system. Prior to the growth of the HCNWs, the silicon substrates were seeded by spin-coating a diamond slurry, which yields high seeding densities in the range up to 10^{10} cm^{-2}.[35] The nanowalls have been fabricated using the following process conditions: gas mixtures H_2, CH_4, B_2H_6, and N_2 with a total flow of 328 sccm; microwave radiation of 2.45 GHz; microwave power up to 1300 W and a process pressure of 50 Torr. The nanowalls were grown for 6 h to reach a thickness of ~3.2 μm, which is estimated from the cross-sectional scanning electron microscopy (SEM) micrograph (Figure S1). The [B]/[C] ratio in the plasma was set to 2000 ppm. During the process, the substrate holder was heated up to 700°C by an induction heater, which was controlled by a thermocouple.

The morphology and the microstructure of the HCNWs were examined using scanning electron microscopy (SEM; EVO-40, Zeiss, Germany) with an accelerating voltage of 10 kV and transmission electron microscopy (TEM; Jeol 2100F) with electron energy loss spectroscopy (EELS; Gatan Enfina) in TEM, respectively. The 3D reconstruction of SEM image was performed by a technique described in http://gwyddion.net/, where the scale of grey colour was calibrated as depth. The crystalline quality of the nanowalls was characterized by using micro-Raman spectroscopy (InVia, Renishaw, UK; λ = 514 nm argon ion laser excitation). The local bonding environment was investigated by X-ray absorption spectroscopy (XAS), performed at room temperature in total electron yield mode at the soft X-ray absorption beamline (BL-1) of the Indus-2 synchrotron radiation source at Raja Ramanna Centre for Advance Technology, Indore, India. . The X-ray photoelectron spectroscopy (XPS) analysis was carried out in Escalab 250 Xi spectroscope (Thermofisher Scientific, UK). The spectra were recorded in the C*1s*, B*1s* and N*1s* energy range, using 20 eV pass energy and 0.1 eV energy step size. The spectroscope is equipped with Al Kα source. Charge compensation was controlled through the

low-energy electron and low energy Ar^+ ions emission by means of a flood gun. The Avantage software for spectral deconvolution was provided by the manufacturer.

EC measurements of the HCNW electrodes were carried out on the Autolab potentiostat-galvanostat PGSTAT302N system (Metrohm, Netherlands). For electrochemical characterization, cyclic voltammetry (CV) was performed in a three-electrode cell with a Pt wire as counter electrode and Ag/AgCl as reference electrode and 5 mM Potassium Ferro/Ferri cyanide in 0.1 M KCl was used as electrolyte. Supercapacitor performance was tested with a similar electrode assembly in 1 M Na_2SO_4 electrolyte within the voltage ranging from 0 V to 0.8 V. The galvanostatic charge-discharge (GCD) was done using the chrono-potentiometry mode, within the predefined cut off voltage range obtained from CV measurements. The electrochemical impedance spectroscopy (EIS) measurements were executed in FRA potential scan mode with the same electrode-electrolyte arrangement. A sinusoidal signal having root mean square value of 10 mV was applied as a perturbation within the frequency range from 0.1 Hz to 100 kHz. The as-obtained Nyquist plots were fitted using the NOVA (version 1.11) software.

RESULTS AND DISCUSSION

The high-resolution SEM of the HCNWs shown in Figure 1a reveals the dense and curled morphological nanowalls of lengths around 1-3 μm. The 3D reconstruction SEM image shown in the inset of Figure 1a discloses that the thickness of nanowalls is around 80 to 100 nm with sharp edges at the top of the nanowalls. This nanowall network results in a high-density valley/pore like formation that appears as darker regions in the 3D SEM image. The carbon K-edge XAS spectrum of HCNWs shown in Figure 1b displays a hybrid carbon structure. A typical sp^2-bonded carbon characteristic peak observed at 285.0 eV (1s → π*) is mainly signified for graphite materials (Figure S2).[36] Moreover, a specific feature of a diamond exciton
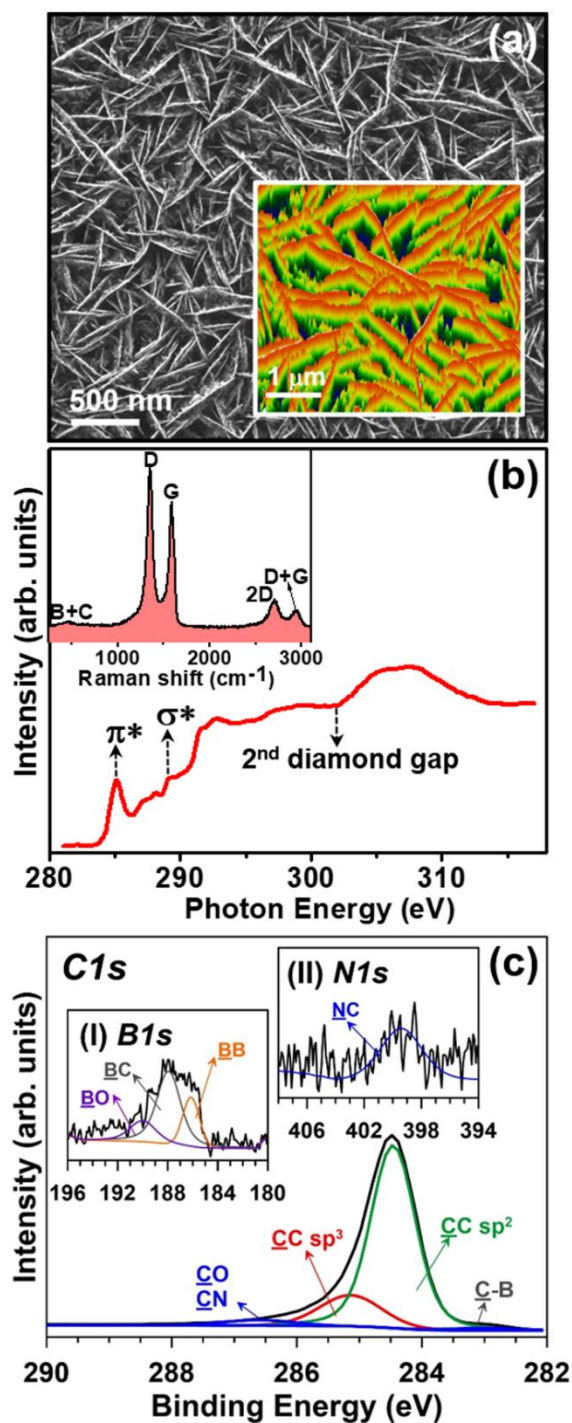
6

Figure 1. (a) SEM micrograph and the corresponding three-dimensional (3D) reconstruction SEM image of HCNWs as inset, (b) normalized C-K edge XAS spectrum with inset of micro-Raman (λ = 514 nm) spectrum of HCNWs, (c) high-resolution XPS spectra for HCNWs recorded for C*1s*, B*1s* (inset I) and N*1s* (inset II) regions.

sharp peak at 289.0 eV and the other specific feature of a dip at 302.5 eV which represents a

second absolute gap in the diamond band structure demonstrate unambiguously the similar

7

features of a single crystalline diamond.[37-39] An additional broad hump centred on 287.0 eV corresponds to chemisorbed oxygen functionalities (C=O).

The inset of Figure 1b illustrates the micro-Raman spectrum of HCNWs. A broad peak at around 480 cm^{-1} is related to boron doping in the HCNWs.[40] A prominent peak of the D band at around 1350 cm^{-1}, which is related with disordered sp^3-hybridized carbon featured as defects or impurities in carbon materials. The G band around 1584 cm^{-1}, which is associated with the E_{2g} phonon modes of the sp^2-bonded carbon. A broad 2D peak around 2700 cm^{-1} originates from a second-order process. The I_{2D}/I_G ratio is about 0.23, indicating that the carbon clusters are ultra-thin multilayered graphene.[41] A (D+G) band at 2938 cm^{-1} is related to the defects in sp^2 sites and a graphene domain edge in the HCNWs.[42] The characteristic diamond peak observed at 1332 cm^{-1} is not seen in the Raman spectrum because micro-Raman spectroscopy is highly sensitive to sp^2 sites, especially for the wavelength employed here. Furthermore, the high-resolution XPS analysis results are presented in Figure 1c. The analysis was performed in order to determine the surface bonding characteristics of HCNWs. In the C$1s$ spectrum, the most notable components are located at binding energy 284.3 and 285.1 eV and could be ascribed to sp^2-carbon and sp^3-carbon, respectively. The spectrum discloses that the carbon clusters are dominated by sp^2 carbon bonding (peak intensity of 74.6%) and sp^3 carbon bonding (peak intensity of 16.7%). The boron incorporation is revealed in the C$1s$ spectrum in the form of an additional deconvolution peak located at 283.1 eV.[43-45] The C-N peak at 286.2 eV (peak intensity of 0.9%) implies the presence of nitrogen in the sample. The level of surface oxidation is small and manifests itself in the form of C$1s$ peak at 286.2 eV characteristic for carbonyl bonds[46-47] but also B$1s$ peak for oxidized boron at 190.0 eV.[44,47] The broad B$1s$ peak (inset I of Figure 1c) was deconvoluted to three components, where the major contribution came from B-C interaction at 187.9 eV and elemental boron at 186.1 eV apart from previously mentioned oxidized boron.[44,48-49] Despite a very high contribution of nitrogen during the CVD process, its

8

low incorporation can be seen on the base of N$1s$ spectrum (inset II of Figure 1c), reaching a peak intensity of 0.4%.

TEM studies were performed to unravel the microstructure of HCNWs. Figure 2a shows the bright field TEM micrograph (BF-TEM) of the HCNWs, indicating that the carbon clusters of nanowall geometry are uniform and densely distributed in the samples. The grains oriented near some zone-axis strongly diffract electrons and show high contrast. High contrast of these carbon clusters implies that they are well crystallized and diffract electrons strongly. The adjacent grains are oriented away from the zone-axis, showing no contrast. A selective area electron diffraction (SAED) pattern shown in the inset of Figure 2a reveals the presence of a strong diffraction ring (designated as "G" and indicated by the arrow), which corresponds to the presence of abundant graphene (G) phase. There also exists a strong diffuse ring in the center of SAED, which corresponds to amorphous carbon, presumably coming from the *trans*-polyacetylene located in the grain boundaries. An extra ring exists near to the (111) ring, corresponding to *n*-diamond, which is a metastable allotropy of diamond with FCC structure and cell parameter of 0.356 nm.[50] A high resolution TEM (HRTEM) micrograph shown in Figure 2b, corresponding to the region 'A' in Figure 2a, discloses the presence of a core-shell granular structure, i.e.- a diamond core encased in a multilayered graphene shell. The Fourier transformed (FT) diffractogram of the whole structure image (FT_{0b}) indicates that the cubic diamond structure (3C diamond) is present, providing the existence of diamond and the donut-shaped diffused diffraction ring located at the center of FT image, which corresponds to graphene phase. A FT image of the designated region "1" (ft_1 image) indicates that, the nanowalls contain mostly the diamond (D) phase along with some multilayered graphene, whereas the ft_2 image of the designated region "2" reveals the presence of graphite (G) phases. Tilting the samples slightly such that the large aggregates "A" gets oriented away from the zone axis, weakly diffracting the electrons and exhibiting low contrast, the microstructure of

the background materials shows up. Interestingly, the BF-TEM image in Figure 2c, which shows the microstructure of the same region as that in Figure 2a, reveals that the HCNWs contain a large number of small carbon clusters (indicated by arrows). This proves that these ultra-small carbon clusters with needle-like geometry are distributed all over the whole region in the large carbon nanowalls, which is in accord with the 3D-SEM micrograph (inset "I" of Figure 1). The SAED pattern in the inset of Figure 2c shows the same features as revealed by the SAED pattern in the inset of Figure 2a. A structure image shown in Figure 2d corresponding
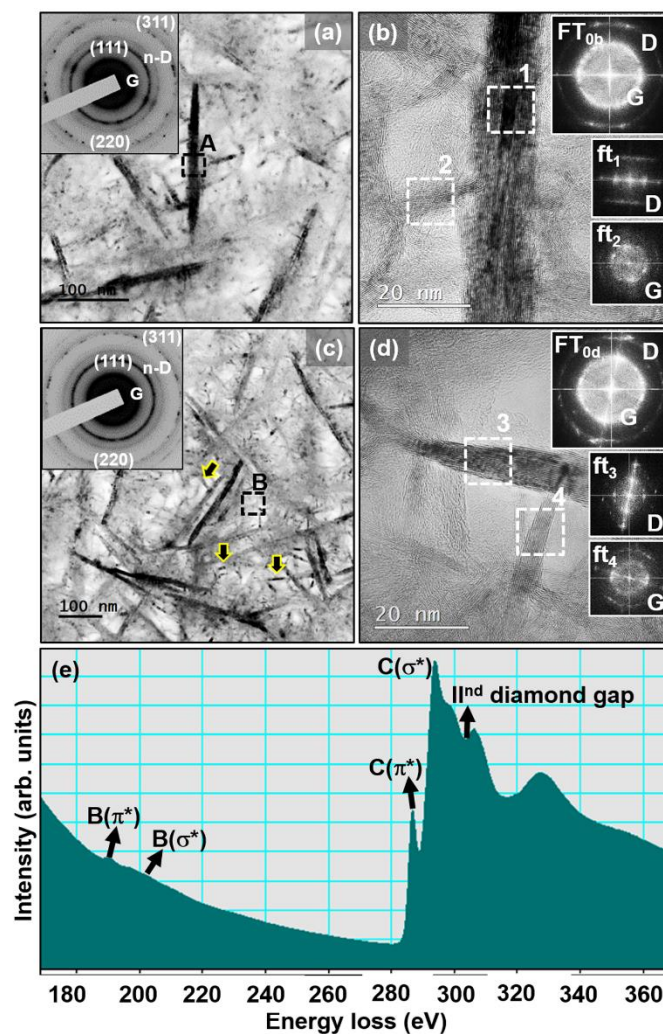

Figure 2. (a) A bright field TEM (BF-TEM) micrograph of the HCNWs, whereas the corresponding SAED pattern is shown as inset. (b) High resolution TEM micrograph taken at the region marked as "A" in "a" with the Fourier transformed diffractogram corresponding to entire structure image shown as inset "FT$_{0b}$". (c) A tilted-view BF-

TEM micrograph of "a" with the corresponding SAED pattern shown as inset. (d) High resolution TEM micrograph taken at the region marked as "B" in "c" with the Fourier transformed diffractogram corresponding to entire structure image shown as inset "FT_{0d}". The ft_1-ft_4 images show the FT images corresponding to regions "1-4" of the structure images, respectively. (e) Boron and carbon core-loss EELS spectrum corresponding to BF-TEM micrograph in "a".

to the marked region "B" in Figure 2c reveals the presence of a sharp edge carbon cluster formed at the tip of core-shell structured grains. The FT_{0d} image corresponding to the entire structure image in Figure 2d contains diffraction spots arranged in a ring and a diffuse diffraction ring at the centre, indicating the co-existence of randomly oriented nano-sized diamond and graphene clusters. The ft_3-image corresponding to region "3" highlights an ultra-small diamond cluster as core with multilayered graphene as shell, whereas the ft_4-image corresponding to region "4" highlights sp^2-bonded graphene phases encasing diamond core. Region "4" contains a larger proportion of diamond, as compared with the region "3", as inferred by the relatively higher intensity of the diamond ring in ft_4.

The local bonding characteristics of these HCNWs are analysed using EELS in TEM. The core-loss EELS spectrum in the boron and carbon K-edge region for HCNWs (Figure 2e), which corresponds to the BF-TEM micrograph in Figure 2a, was recorded. The features of the B K-edge EELS are dominated by a sharp peak at ~195.0 eV assigned to the transition of boron 1s electrons to unoccupied π^* states, similar to the case of carbon. A broad peak at ~205.0 eV represents the transition of boron 1s electrons to unoccupied B–C or B–B sigma anti-bonding σ^* states.[51] In the case of C K-edge EELS, a sharp peak at 289.5 eV (σ^* band) and a dip valley in the vicinity of 302.0 eV signify the sp^3-bonded carbon (the diamond).[52] A large bump occurs at 285.0 eV (π^* band) representing sp^2-bonded carbon.[52-54] Hence, the microscopic and spectroscopic results imply that HCNW is actually a nanocarbon hybrid material, consisting of diamond as core and multilayered graphene as shell.

11

The growth process of HCNWs involves H^+, H_yCNH_x, BH_x, CH^+_x and C_2 species in the plasma, which are responsible for such a developed the nanowall-like structure formation.[45,55] The diamond core of the nanowalls originates from overgrown nanodiamond grains used for the seeding. The CH^+_x radicals and C_2 are mostly presumed to be the growing species for diamond. The new diamond clusters renucleated frequently due to the presence of abundant C_2 species in the plasma, ensuing in ultra-small diamond grains.[56] Furthermore, BH_x and H_yCNH_x radicals were mainly responsible for the developed nanowall morphology attributed to the twinning surface processes,[57] which might be originated from the formation of a boron rich cluster. Thus, graphene shells are ascribed to the degenerated growth of diamond phases caused predominantly by BH_x and HCN species.[45]

To gain insight into the intrinsic electrochemical activity of HCNWs, first the electron transfer kinetics of HCNW electrodes were investigated employing a electrochemical redox couple ($[Fe(CN)_6]^{3-/4-}$ in 0.1M KCl) in cyclic voltammetry (CV) measurements. Undoped carbon nanowalls (UCNWs) were also used for comparison. The fabrication of UCNWs was described elsewhere.[58] It is known that redox couple $[Fe(CN)_6]^{3-/4-}$ does not involve simple electron transfer to metal or carbon electrode where electrodes act as a source and sink of electrons. Especially for carbon based electrodes, the electron transfer kinetics are strongly depending on the edge plane exposed on sp^2 bonded carbon and the reaction rate is increased proportionally with the exposed edge planes.[59-60] In addition, the electron transfer kinetics are also very sensitive to the surface oxygen functionalities. Numerous reports have revealed the degree of reversibility of a redox reaction; i.e. the anodic and cathodic peak potential separation (ΔE_p) is much larger in case of an oxygen terminated surface and can be reduced by removing the oxygen functionalities.[61] Here, the ΔE_p values for HCNWs and UCNWs obtained from the cyclic voltammetry curves (Figure S3a) are 276 mV and 415 mV respectively. Therefore, low ΔE_p and high peak currents ($i_{p,a}/i_{p,c}$ = 295.44/286.43 µA) for HCNWs might be due to the larger

fraction of exposed edge planes of sp^2 bonded carbon and less surface carbon-oxygen functionalities (i.e. carboxyl groups) as confirmed by Raman, XAS and XPS analyses. The coulombic efficiency ($\eta\%$) of the electrode materials i.e. the ratio of cathodic to anodic peak current, also shows a greater value for HCNW (96.9 %) over UCNW electrodes (92.6 %) indicating a high charge retention of the $[Fe(CN)_6]^{3-/4-}$ redox couple in 0.1 M KCl solution. Moreover, a significant drop in the half-cell potential (to 230 mV) for HCNWs as compared to UCNWs (~456 mV), implies an improved electrode stability of HCNW. It can be analysed from the scan rate dependence CV curves for the HCNW electrodes (Figure S3b) that both anodic and cathodic peak currents are proportional to the square root of the scan rate (inset of Figure S3b) and the ΔE_p value increases with increasing scan rate. These results are consistent with the results for quasi reversible redox systems using glassy carbon electrodes.[62-63] The electrochemical parameters calculated from CV curves are summarized in Table S1. The electrochemical results designate that the HCNWs possess the desired properties with requisite surface structure, chemical bonding environment and electronic properties in support of quick electron transfer. Therefore, a 3D porous network of HCNWs with sp^2 carbon rich edge sites contribute more significantly to fast electron transfer kinetics as compared to UCNWs and can be beneficially employed as a working electrode material for supercapacitor applications.

In order to evaluate the supercapacitive performance of the HCNW, CV curves were recorded for both the electrodes, the HCNWs (Figure 3a) and UCNWs (Figure S4a) in 1M Na_2SO_4 aqueous solution with varying scan rates. As expected, the capacitive current enhances with increasing scan rates and the CV curves show a symmetrical parallelogram shape, signifying a practical EDLC type capacitive behaviour for both the electrodes. This appears due to faster charging/discharging of exterior surface than the pores in nanowall electrode.[64-65] A significant enhancement in the current and the integrated area under the CV curve is noticed in HCNW compared to the undoped ones (for comparison, CV curves are overlapped for both the

electrodes in Figure S4(b). The double layer capacitance is calculated from the enclosed area under the CV curve using the following equation,

$$C = \frac{1}{2} \frac{\int I\,(V)dV}{\Delta V \times \vartheta \times A}$$

-----------------------------(1)

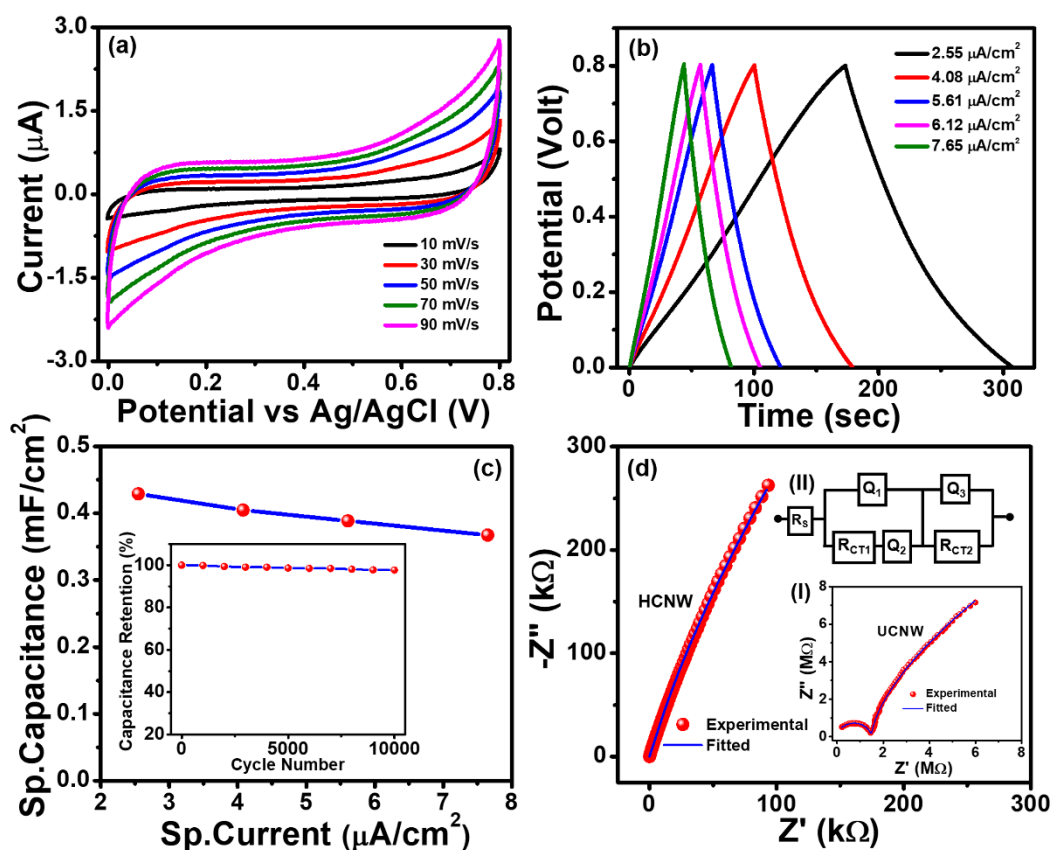**Figure 3.** Supercapacitor performance of HCNWs in 1M Na_2SO_4 aqueous solution: (a) Cyclic voltammograms at the scan rate varying from 10-90 mV s^{-1}, (b) galvanostatic charge-discharge curves at current densities from 2.55-7.65 µA cm^{-2} in a potential window of 0-0.8 V, (c) variation of specific capacitance with specific current and inset shows percentage of capacitance retention as a function of charge-discharge cycles at 2.55 µA cm^{-2} current density, (d) experimental and fitted impedance spectra for HCNWs, inset I shows the corresponding impedance spectra of UCNWs and inset II shows the equivalent electrical circuit model.

where, $\int I\,(V)dV$ is the total current enclosed, ΔV is the potential window and ϑ is the scan rate, A is the geometrical area of the capacitor electrode. The capacitance value for HCNW was found to be ~ 94 µF cm^{-2} at a scan rate of 10 mV s^{-1}, whereas for the UCNWs, the value reached only ~38.9 µF cm^{-2}. The obtained specific capacitance values at different scan rates

MOST WIEDZY Downloaded from mostwiedzy.pl

for both electrodes are shown in Figure S4c indicating a good capacitive behaviour and a fast-ionic diffusion in the pores of the HCNWs. Whereas, a poor capacitive performance is observed for the undoped material, which could be attributed to the poor electrical conductivity.

In the next step, the galvanostatic charge-discharge (GCD) method was employed to determine the specific capacitance and cyclic stability of the HCNW electrode within the same potential range obtained from CV (0 - 0.8 V versus Ag/AgCl ref. electrode) using 1 M Na_2SO_4 as electrolyte. The equation employed to find out specific capacitance from GCD is

$$C = \frac{1}{2}\frac{I \times \Delta t}{\Delta V \times A} \qquad \text{------------------------------(2)}$$

Where, I is the capacitive current obtained from GCD, Δt is charge and discharge time, ΔV is the scanned potential window, A is the effective geometrical area of the capacitor electrode. GCD curves for HCNWs at current densities ranging from 2.55 to 7.65 μA cm^{-2} (Figure 3b) show linear and symmetric nature during charging and discharging cycles, which delineate an excellent stable capacitive characteristic and high reversibility of the electrode. With increasing current density, the time required for one charge cycle is becoming less. For comparison, the GCD curves of both HCNWs and UCNWs are represented in Figure S4d, which also suggests the superiority of HCNWs over UCNWs in terms of charge storage capability by higher charge-discharge duration. The value of specific capacitance calculated from GCD curve was found to be ~ 0.43 mF cm^{-2} for HCNWs, whereas it is merely 32.5 μF cm^{-2} for undoped ones at the current density 2.55 μA cm^{-2}. The quantified values of specific capacitances of HCNWs at different current densities using equation 2 are plotted in Figure 3c. As a key factor of utilization of HCNW for EDLC applications, charging/discharging was carried out again in 1M Na_2SO_4 at a current density of 2.55 μA cm^{-2} to evaluate the capacitance retention or cyclic stability of the HCNW. The variation of capacitance retention as a function of cycle number is plotted in the inset of Figure 3c. A remarkable retention (~97.6%) after 10000 cycles can be

15

seen which demonstrates an outstanding stability of the electrodes. The specific capacitance

value obtained from Figure 3b is listed and compared with other electrode materials in Table

1.

Table 1 The specific capacitance values of HCNW electrodes compared to the other electrode

materials in different electrolytes reported in literature.

Capacitor Electrodes	Electrolyte	Capacitance ($\mu F/cm^2$)
Carbon nanotubes[66-67]	Organic electrolyte	5–9
Graphene[68]	Aqueous	10–40
Graphene[67-69]	Organic electrolyte	4–14
Activated carbon[67]	Aqueous	3–15
Nanodiamond[66]	NEt_4BF_4/acetonitrile	4
Boron doped diamond (BDD)[29]	Na_2SO_4	3.6–7
BDD[70]	KCl	15.1
BDD[70]	BMIMBF4	10.9
Diamond[71]	Tetraethylammonium tetrafluoroborate (Et4NBF4)/Propylene carbonate (PC)	15.2
Diamond[71]	1 M H_2SO_4	10.3
N-doped ultrananocrystalline diamond[72]	Phosphate buffered saline (PBS, NaCl)	17
Silicon nanowires[73-75]	NEt_4BF_4/PC, PYR13 TFSI	23–50
Silicon nanotrees[76]	NEt4BF4/ PC	84
Diamond-coated silicon wire[77]	PMPyrrTFSI/PC	105
Diamond foam[78]	PMPyrrTFSI/PC	0.43×10^3
Diamond foam[78]	$NaClO_4$	0.5×10^3
Diamond paper[79]	$NaClO_4$	0.6×10^3
HCNWs[This work]	Na_2SO_4	0.43×10^3

Finally, we performed electrochemical impedance spectroscopy (EIS) studies in 1 M Na_2SO_4

to evaluate the impedance and electrode kinetics of the HCNW and UCNW electrodes.[80] In

order to understand the charge transfer kinetics and ionic diffusion of the electrodes, a Nyquist plot is obtained for both the electrodes (Figure 3d), where the real part of the impedance is plotted as a function of its imaginary part. The diameter of the semi-circular part in the impedance spectra provides the qualitative description about the magnitude of the charge transfer resistance of the system[81] where a higher diameter signifies a high charge transfer resistance. The small semi-circular region in the HCNW electrodes indicates better charge transfer kinetics as compared to the UCNWs (inset I of Figure 3d) and further confirms a higher electrical conductivity in the HCNWs sample.

An equivalent electrical circuit was modelled and is represented in the inset II of Figure 3d. The circuit can be classified into three distinct parts. The first part of the circuit is constructed using a series resistance (R_S), which takes care of solution resistance and contact resistance. The second and third part of the circuit is consisting of charge transfer resistances and constant phase elements (CPE). The charge transfer resistance arises due to the fast-faradic reaction at electrode-electrolyte interface. The variation in potential, non-linearity and inhomogeneity in the system lead to include CPE in the model circuit which is a mixture of resistance and capacitance. The CPE (Q) can be denoted as: $Q = Y_o(j\omega)^{-\alpha}$, where $Y_o = {1}/{C}$ for $\alpha = 1$ and, $Y_o = R$ for $\alpha = 0$; C and R represents the capacitance and resistance respectively. α is labelled as the exponent of CPE. For a zero value of α the component is purely resistive and for $\alpha = 1$, the component is purely capacitive. The second portion of the equivalent circuit represents the electrode kinetics of the electrode material. In the circuit representation of this region, Q_1 arises due to the diamond nanostructure and Q_2 corresponds to the silicon substrate. These kinds of model circuits can also be found in other reports.[82-84] The last part of the equivalent circuit is a parallel combination of a charge transfer resistance (R_{CT2}) and Q_3, and can be correlated with the electrode kinetics of the electrode and electrolyte interface and is already reported in the

17

literature.[85] The goodness of fit (χ^2) for UCNWs and HCNWs are calculated as 0.03 and 0.02, respectively, implying an excellent fitting.

The circuit parameters extracted from the model equivalent circuits are represented in Table S2. The series resistance (R_s) for the HCNW specimen was found to be ~66.3 Ω which was much lower as compared to the simple UCNW (~200 Ω). The charge transfer resistance (R_{CT1}) for the undoped sample was calculated as ~1000 Ω. But a substantial 10-fold decrease in the charge transfer resistance and the R_{CT1} value of 100 Ω was evaluated for the HCNW sample. The minimal series and charge transfer resistance in the HCNWs can be attributed to both the doped diamond core and the multilayered graphene shell, which collectively enhanced the electronic conductivity. Such hybrid nanostructure is also found to be beneficial in dragging the charge transfer resistance between the electrode and electrolyte (R_{CT2} ~1 kΩ) well below that of the UCNW sample (~1.48 MΩ).

Thus, the better supercapacitor performance of the HCNW electrodes can be correlated with the presence of electrochemically stable diamond nanowalls and graphene encapsulation layers where graphene is boosting energy storage capacity in the HCNW, by providing large specific surface area and enhancing charge transfer kinetics. However, we believe that performance of such hybrid material can be improved in future by optimizing the pore size distribution, incorporating pentavalent impurities (such as nitrogen, phosphorus etc. instead of boron), by surface termination (H_2, O_2, N_2 etc.) and incorporation of some pseudocapacitive material (such as TiO_2, MnO_2, etc.).

Conclusions

A facile way of fabricating HCNWs and the efficacy of this material as electrode for developing energy storage systems have been demonstrated. The hybrid nanowall electrodes evince high capacitance value, long term capacitance retention, supported by electrochemical

measurements like CV, GCD, etc. Such brilliant performance is ascribed to the formation of the 3D nanowall geometry, a large surface area, and an improved electrical conductivity. The nanowall morphology was confirmed by SEM, whereas XPS, Raman, XAS, TEM and EELS unveil the inclusion of boron as well as co-occurrence of diamond and graphene, with the former as a core encased in a multilayered graphene shell. Such clever engineering of graphene on diamond might helped to enhance the available surface area for electrolyte reaction, charge carrier mobility. All these together create an improved interphase/interfacial dynamic of physicochemical processes. This study could expectantly spread out the extent and freedom of implementation of new hybrid diamond materials for future energy storage devices.

Supporting Information

Electrochemical parameters obtained from cyclic voltammetry measurements of HCNWs and UCNWs electrodes in 0.1M KCl containing 5mM $[Fe(CN)_6]^{3-/4}$ (Table S1), Circuit parameters for model equivalent circuit obtained from EIS of HCNWs and UCNWs (Table S2), Cross-sectional scanning electron micrograph of HCNW (Figure S1), XAS spectrum of graphite (Figure S2), Electrochemical performance of the HCNW and UCNW electrodes in 0.1M KCl containing 5 mM $[Fe(CN)_6]^{3-/4}$ (Figure S3), Comparison of supercapacitor performance of HCNW and UCNW electrodes in 1M Na_2SO_4 (Figure S4).

Conflict of Interest

There are no conflicts to declare.

References

1. Tarascon, J.-M.; Armand, M., Issues and Challenges Facing Rechargeable Lithium Batteries. In *Materials for Sustainable Energy*, pp 171-179.

2. Holze, R., F. Béguin, E. Frąckowiak (Eds): Supercapacitors – Materials, Systems, and Applications. *J. Solid State Electrochem.* **2015**, *19*, 1253-1253.

3. Miller, J. R.; Simon, P., Electrochemical Capacitors for Energy Management. *Science Magazine* **2008**, *321*, 651-652.

4. SIMON, P.; GOGOTSI, Y., Materials for Electrochemical Capacitors. In *Nanoscience and Technology*, pp 320-329.

5. Qu, J.; Li, Y.; Lv, S.; Gao, F.; Geng, C.; Wu, M., Dense 3d Graphene Macroforms with Nanotuned Pore Sizes for High Performance Supercapacitor Electrodes. *J. Phys. Chem. C* **2015**, *119*, 24373-24380.

6. El-Kady, M. F.; Kaner, R. B., Scalable Fabrication of High-Power Graphene Micro-Supercapacitors for Flexible and on-Chip Energy Storage. *Nature Comm.* **2013**, *4*, 1475.

7. Peng, Z.; Lin, J.; Ye, R.; Samuel, E. L. G.; Tour, J. M., Flexible and Stackable Laser-Induced Graphene Supercapacitors. *ACS Appl. Mater. Interfaces* **2015**, *7*, 3414-3419.

8. El-Kady, M. F.; Strong, V.; Dubin, S.; Kaner, R. B., Laser Scribing of High-Performance and Flexible Graphene-Based Electrochemical Capacitors. *Science* **2012**, *335*, 1326.

9.   Hsia, B.; Marschewski, J.; Wang, S.; In, J. B.; Carraro, C.; Poulikakos, D.; Grigoropoulos, C. P.; Maboudian, R., Highly Flexible, All Solid-State Micro-Supercapacitors from Vertically Aligned Carbon Nanotubes. *Nanotechnol.* **2014**, *25*, 055401.

10.   Lin, J.; Zhang, C.; Yan, Z.; Zhu, Y.; Peng, Z.; Hauge, R. H.; Natelson, D.; Tour, J. M., 3-Dimensional Graphene Carbon Nanotube Carpet-Based Microsupercapacitors with High Electrochemical Performance. *Nano Lett.* **2013**, *13*, 72-78.

11.   Pech, D.; Brunet, M.; Taberna, P.-L.; Simon, P.; Fabre, N.; Mesnilgrente, F.; Conédéra, V.; Durou, H., Elaboration of a Microstructured Inkjet-Printed Carbon Electrochemical Capacitor. *J. Power Sources* **2010**, *195*, 1266-1269.

12.   Abbas, Q.; Ratajczak, P.; Babuchowska, P.; Le Comte, A.; Bélanger, D.; Brousse, T.; Béguin, F., Strategies to Improve the Performance of Carbon/Carbon Capacitors in Salt Aqueous Electrolytes. *J. Electrochem. Soc.* **2015**, *162*, A5148-A5157.

13.   Rudge, A.; Davey, J.; Raistrick, I.; Gottesfeld, S.; Ferraris, J. P., Conducting Polymers as Active Materials in Electrochemical Capacitors. *J. Power Sources* **1994**, *47*, 89-107.

14.   Sun, W.; Chen, X., Fabrication and Tests of a Novel Three Dimensional Micro Supercapacitor. *Microelectronic Engg.* **2009**, *86*, 1307-1310.

15.   Brezesinski, T.; Wang, J.; Tolbert, S. H.; Dunn, B., Ordered Mesoporous A-Moo 3 with Iso-Oriented Nanocrystalline Walls for Thin-Film Pseudocapacitors. *Nature mater.* **2010**, *9*, 146.

16.   Mishra, A. K.; Nayak, A. K.; Das, A. K.; Pradhan, D., Microwave-Assisted Solvothermal Synthesis of Cupric Oxide Nanostructures for High-Performance Supercapacitor. *J. Phys. Chem. C* **2018**, *122*, 11249-11261.

17.   Yoo, J. J., et al., Ultrathin Planar Graphene Supercapacitors. *Nano Lett.* **2011**, *11*, 1423-1427.

18.   Wang, X.; Myers, B. D.; Yan, J.; Shekhawat, G.; Dravid, V.; Lee, P. S., Manganese Oxide Micro-Supercapacitors with Ultra-High Areal Capacitance. *Nanoscale* **2013**, *5*, 4119-4122.

19.   Shen, C.; Wang, X.; Li, S.; Wang, J. g.; Zhang, W.; Kang, F., A High-Energy-Density Micro Supercapacitor of Asymmetric Mno2–Carbon Configuration by Using Micro-Fabrication Technologies. *J. Power Sources* **2013**, *234*, 302-309.

20.   Wu, Z.-S.; Parvez, K.; Li, S.; Yang, S.; Liu, Z.; Liu, S.; Feng, X.; Müllen, K., Alternating Stacked Graphene-Conducting Polymer Compact Films with Ultrahigh Areal and Volumetric Capacitances for High-Energy Micro-Supercapacitors. *Adv. Mater.* **2015**, *27*, 4054-4061.

21.   Dinh, T. M.; Achour, A.; Vizireanu, S.; Dinescu, G.; Nistor, L.; Armstrong, K.; Guay, D.; Pech, D., Hydrous Ruo2/Carbon Nanowalls Hierarchical Structures for All-Solid-State Ultrahigh-Energy-Density Micro-Supercapacitors. *Nano Energy* **2014**, *10*, 288-294.

22.   Simon, P.; Gogotsi, Y., Materials for Electrochemical Capacitors. *Nature Mater.* **2008**, *7*, 845.

23.   Wang, G.; Zhang, L.; Zhang, J., A Review of Electrode Materials for Electrochemical Supercapacitors. *Chem. Soc. Rev.* **2012**, *41*, 797-828.

24.   Zhang, L. L.; Zhao, X. S., Carbon-Based Materials as Supercapacitor Electrodes. *Chem. Soc. Rev.* **2009**, *38*, 2520-2531.

25.   Yang, N.; Foord, J. S.; Jiang, X., Diamond Electrochemistry at the Nanoscale: A Review. *Carbon* **2016**, *99*, 90-110.

26.   Shalini, J.; Sankaran, K. J.; Dong, C.-L.; Lee, C.-Y.; Tai, N.-H.; Lin, I.-N., In Situ Detection of Dopamine Using Nitrogen Incorporated Diamond Nanowire Electrode. *Nanoscale* **2013**, *5*, 1159-1167.

27.	Yang, N.; Yu, S.; Macpherson, J. V.; Einaga, Y.; Zhao, H.; Zhao, G.; Swain, G. M.; Jiang, X., Conductive Diamond: Synthesis, Properties, and Electrochemical Applications. *Chem. Soc. Rev.* **2019**, *48*, 157-204.

28.	Yu, S.; Yang, N.; Vogel, M.; Mandal, S.; Williams, O. A.; Jiang, S.; Schönherr, H.; Yang, B.; Jiang, X., Battery-Like Supercapacitors from Vertically Aligned Carbon Nanofiber Coated Diamond: Design and Demonstrator. *Adv. Energy Mater.* **2018**, *8*, 1702947.

29.	Yu, S.; Yang, N.; Zhuang, H.; Meyer, J.; Mandal, S.; Williams, O. A.; Lilge, I.; Schönherr, H.; Jiang, X., Electrochemical Supercapacitors from Diamond. *J. Phys. Chem. C* **2015**, *119*, 18918-18926.

30.	Garrett, D. J.; Ganesan, K.; Stacey, A.; Fox, K.; Meffin, H.; Prawer, S., Ultra-Nanocrystalline Diamond Electrodes: Optimization Towards Neural Stimulation Applications. *J. Neural Engg.* **2011**, *9*, 016002.

31.	Hébert, C., et al., Boron Doped Diamond Biotechnology: From Sensors to Neurointerfaces. *Faraday Discussions* **2014**, *172*, 47-59.

32.	Smirnov, W.; Kriele, A.; Yang, N.; Nebel, C. E., Aligned Diamond Nano-Wires: Fabrication and Characterisation for Advanced Applications in Bio- and Electrochemistry. *Diamond Relat. Mater.* **2010**, *19*, 186-189.

33.	Janssen, W.; Faby, S.; Gheeraert, E., Bottom–up Fabrication of Diamond Nanowire Arrays. *Diamond Relat. Mater.* **2011**, *20*, 779-781.

34.	Siuzdak, K.; Bogdanowicz, R., Nano-Engineered Diamond-Based Materials for Supercapacitor Electrodes: A Review. *Energy Technol.* **2018**, *6*, 223-237.

35.	Bogdanowicz, R.; Sobaszek, M.; Ryl, J.; Gnyba, M.; Ficek, M.; Gołuński, Ł.; Bock, W. J.; Śmietana, M.; Darowicki, K., Improved Surface Coverage of an Optical Fibre with Nanocrystalline Diamond by the Application of Dip-Coating Seeding. *Diamond Relat. Mater.* **2015**, *55*, 52-63.

36.   Fayette, L.; Marcus, B.; Mermoux, M.; Tourillon, G.; Laffon, K.; Parent, P.; Le Normand, F., Local Order in Cvd Diamond Films : Comparative Raman, X-Ray-Diffraction, and X-Ray-Absorption near-Edge Studies. *Phys. Rev. B* **1998**, *57*, 14123-14132.

37.   Birrell, J.; Gerbi, J. E.; Auciello, O.; Gibson, J. M.; Gruen, D. M.; Carlisle, J. A., Bonding Structure in Nitrogen Doped Ultrananocrystalline Diamond. *J. Appl. Phys.* **2003**, *93*, 5606-5612.

38.   Chang, Y. K., et al., Quantum Confinement Effect in Diamond Nanocrystals Studied by X-Ray-Absorption Spectroscopy. *Phys. Rev. Lett.* **1999**, *82*, 5377-5380.

39.   Joseph, P. T.; Tai, N. H.; Chen, C. H.; Niu, H.; Cheng, H. F.; Pong, W. F.; Lin, I. N., On the Mechanism of Enhancement on Electron Field Emission Properties for Ultrananocrystalline Diamond Films Due to Ion Implantation. *J. Phys. D: Appl. Phys.* **2009**, *42*, 105403.

40.   Polyakov, S. N.; Denisov, V. N.; Mavrin, B. N.; Kirichenko, A. N.; Kuznetsov, M. S.; Martyushov, S. Y.; Terentiev, S. A.; Blank, V. D., Formation of Boron-Carbon Nanosheets and Bilayers in Boron-Doped Diamond: Origin of Metallicity and Superconductivity. *Nanoscale Res. Lett.* **2016**, *11*, 11.

41.   Ferrari, A. C., et al., Raman Spectrum of Graphene and Graphene Layers. *Phys. Rev. Lett.* **2006**, *97*, 187401.

42.   Kalita, G.; Wakita, K.; Umeno, M., Low Temperature Growth of Graphene Film by Microwave Assisted Surface Wave Plasma Cvd for Transparent Electrode Application. *RSC Adv.* **2012**, *2*, 2815-2820.

43.   Sun, Y.; Meng, Q.; Qian, M.; Liu, B.; Gao, K.; Ma, Y.; Wen, M.; Zheng, W., Enhancement of Oxidation Resistance Via a Self-Healing Boron Carbide Coating on Diamond Particles. *Sci. Rep.* **2016**, *6*, 20198.

44.   Wan, S.; Yu, Y.; Pu, J.; Lu, Z., Facile Fabrication of Boron Nitride Nanosheets– Amorphous Carbon Hybrid Film for Optoelectronic Applications. *RSC Adv.* **2015**, *5*, 19236-19240.

45.   Sobaszek, M.; Siuzdak, K.; Ryl, J.; Sawczak, M.; Gupta, S.; Carrizosa, S. B.; Ficek, M.; Dec, B.; Darowicki, K.; Bogdanowicz, R., Diamond Phase (Sp3-C) Rich Boron-Doped Carbon Nanowalls (Sp2-C): Physicochemical and Electrochemical Properties. *J. Phys. Chem. C* **2017**, *121*, 20821-20833.

46.   Ryl, J.; Zielinski, A.; Burczyk, L.; Bogdanowicz, R.; Ossowski, T.; Darowicki, K., Chemical-Assisted Mechanical Lapping of Thin Boron-Doped Diamond Films: A Fast Route toward High Electrochemical Performance for Sensing Devices. *Electrochim. Acta* **2017**, *242*, 268-279.

47.   Kolel-Veetil, M. K.; Gamache, R. M.; Bernstein, N.; Goswami, R.; Qadri, S. B.; Fears, K. P.; Miller, J. B.; Glaser, E. R.; Keller, T. M., Substitution of Silicon within the Rhombohedral Boron Carbide (B4c) Crystal Lattice through High-Energy Ball-Milling. *J. Mater. Chem. C* **2015**, *3*, 11705-11716.

48.   Frank, L. P.; Yun, L.; Jincheng, D.; Jeffry, A. K., Novel Alloy Polymers Formed from Ortho -Carborane and Benzene or Pyridine. *J. Phys.: Cond. Matt.* **2013**, *25*, 105801.

49.   Sadhanala, H. K.; Nanda, K. K., Boron-Doped Carbon Nanoparticles: Size-Independent Color Tunability from Red to Blue and Bioimaging Applications. *Carbon* **2016**, *96*, 166-173.

50.   Ficek, M.; Sankaran, K. J.; Ryl, J.; Bogdanowicz, R.; Lin, I.-N.; Haenen, K.; Darowicki, K., Ellipsometric Investigation of Nitrogen Doped Diamond Thin Films Grown in Microwave Ch4/H2/N2 Plasma Enhanced Chemical Vapor Deposition. *Appl. Phys. Lett.* **2016**, *108*, 241906.

51.   Lu, Y.-G.; Turner, S.; Verbeeck, J.; Janssens, S. D.; Haenen, K.; Tendeloo, G. V., Local Bond Length Variations in Boron-Doped Nanocrystalline Diamond Measured by Spatially Resolved Electron Energy-Loss Spectroscopy. *Appl. Phys. Lett.* **2013**, *103*, 032105.

52.   Kovarik, P.; Bourdon, E. B. D.; Prince, R. H., Electron-Energy-Loss Characterization of Laser-Deposited a-C, a-C:H, and Diamond Films. *Phys. Rev. B* **1993**, *48*, 12123-12129.

53.   Sankaran, K. J.; Huang, B.-R.; Saravanan, A.; Manoharan, D.; Tai, N.-H.; Lin, I.-N., Nitrogen Incorporated Ultrananocrystalline Diamond Microstructures from Bias-Enhanced Microwave N2/Ch4-Plasma Chemical Vapor Deposition. *Plas. Proc. Polym.* **2016**, *13*, 419-428.

54.   Prawer, S.; Peng, J. L.; Orwa, J. O.; McCallum, J. C.; Jamieson, D. N.; Bursill, L. A., Size Dependence of Structural Stability in Nanocrystalline Diamond. *Phys. Rev. B* **2000**, *62*, R16360-R16363.

55.   Sankaran, K. J., et al., Self-Organized Multi-Layered Graphene–Boron-Doped Diamond Hybrid Nanowalls for High-Performance Electron Emission Devices. *Nanoscale* **2018**, *10*, 1345-1355.

56.   Sankaran, K. J.; Srinivasu, K.; Chen, H. C.; Dong, C. L.; Leou, K. C.; Lee, C. Y.; Tai, N. H.; Lin, I. N., Improvement in Plasma Illumination Properties of Ultrananocrystalline Diamond Films by Grain Boundary Engineering. *J. Appl. Phys.* **2013**, *114*, 054304.

57.   Butler, J. E.; Oleynik, I., A Mechanism for Crystal Twinning in the Growth of Diamond by Chemical Vapour Deposition. *Philosophical Transactions of the Royal Society A: Mathematical, Physical and Engineering Sciences* **2008**, *366*, 295-311.

58.   Rani, R.; Panda, K.; Kumar, N.; Sankaran, K. J.; Pandian, R.; Ficek, M.; Bogdanowicz, R.; Haenen, K.; Lin, I. N., Triboenvironment Dependent Chemical Modification of Sliding Interfaces in Ultrananocrystalline Diamond Nanowall Film: Correlation with Friction and Wear. *J. Phys. Chem. C* **2018**, *122*, 945-956.

59.   Granger, M. C., et al., Standard Electrochemical Behavior of High-Quality, Boron-Doped Polycrystalline Diamond Thin-Film Electrodes. *Anal. Chem.* **2000**, *72*, 3793-3804.

60.   Chen, P.; McCreery, R. L., Control of Electron Transfer Kinetics at Glassy Carbon Electrodes by Specific Surface Modification. *Anal. Chem.* **1996**, *68*, 3958-3965.

61.   Granger, M. C.; Swain, G. M., The Influence of Surface Interactions on the Reversibility of Ferri/Ferrocyanide at Boron-Doped Diamond Thin-Film Electrodes. *J. Electrochem. Soc.* **1999**, *146*, 4551-4558.

62.   Hu, I.-F.; Karweik, D. H.; Kuwana, T., Activation and Deactivation of Glassy Carbon Electrodes. *J. Electroanal. Chem. Interfacial Electrochem.* **1985**, *188*, 59-72.

63.   Sundberg, K. M.; Atanasoska, L.; Atanasoski, R.; Smyrl, W. H., Oxygen Reduction of Glassy Carbon in 0.1 M Hcl: Rde and Xps Study. *J. Electroanal. Chem. Interfacial Electrochem.* **1987**, *220*, 161-168.

64.   Tanahashi, I., Comparison of the Characteristics of Electric Double-Layer Capacitors with an Activated Carbon Powder and an Activated Carbon Fiber. *J. Appl. Electrochem.* **2005**, *35*, 1067-1072.

65.   Arof, A.; Shuhaimi, N.; Alias, N.; Kufian, M.; Majid, S., Application of Chitosan/Iota-Carrageenan Polymer Electrolytes in Electrical Double Layer Capacitor (Edlc). *J. Solid State Electrochem.* **2010**, *14*, 2145-2152.

66.   Portet, C.; Yushin, G.; Gogotsi, Y., Electrochemical Performance of Carbon Onions, Nanodiamonds, Carbon Black and Multiwalled Nanotubes in Electrical Double Layer Capacitors. *Carbon* **2007**, *45*, 2511-2518.

67.   Gu, W.; Yushin, G., Review of Nanostructured Carbon Materials for Electrochemical Capacitor Applications: Advantages and Limitations of Activated Carbon, Carbide-Derived Carbon, Zeolite-Templated Carbon, Carbon Aerogels, Carbon Nanotubes, Onion-Like Carbon, and Graphene. *WIRES: Energy Environ.* **2014**, *3*, 424-473.

68.   Stoller, M. D.; Park, S.; Zhu, Y.; An, J.; Ruoff, R. S., Graphene-Based Ultracapacitors. *Nano Lett.* **2008**, *8*, 3498-3502.

69.   Zhu, Y., et al., Carbon-Based Supercapacitors Produced by Activation of Graphene. *Science* **2011**, *332*, 1537.

70.   Kim, D. Y.; Yang, J. C.; Kim, H. W.; Swain, G. M., Heterogeneous Electron-Transfer Rate Constants for Ferrocene and Ferrocene Carboxylic Acid at Boron-Doped Diamond Electrodes in a Room Temperature Ionic Liquid. *Electrochim. Acta* **2013**, *94*, 49-56.

71.   Yoshimura, M.; Honda, K.; Kondo, T.; Uchikado, R.; Einaga, Y.; Rao, T. N.; Tryk, D. A.; Fujishima, A., Factors Controlling the Electrochemical Potential Window for Diamond Electrodes in Non-Aqueous Electrolytes. *Diamond Relat. Mater.* **2002**, *11*, 67-74.

72.   Tong, W., et al., Optimizing Growth and Post Treatment of Diamond for High Capacitance Neural Interfaces. *Biomater.* **2016**, *104*, 32-42.

73.   Aradilla, D.; Gentile, P.; Bidan, G.; Ruiz, V.; Gómez-Romero, P.; Schubert, T. J. S.; Sahin, H.; Frackowiak, E.; Sadki, S., High Performance of Symmetric Micro-Supercapacitors Based on Silicon Nanowires Using N-Methyl-N-Propylpyrrolidinium Bis(Trifluoromethylsulfonyl)Imide as Electrolyte. *Nano Energy* **2014**, *9*, 273-281.

74.   Thissandier, F.; Pauc, N.; Brousse, T.; Gentile, P.; Sadki, S., Micro-Ultracapacitors with Highly Doped Silicon Nanowires Electrodes. *Nanoscale Res. Lett.* **2013**, *8*, 38.

75.   Thissandier, F.; Le Comte, A.; Crosnier, O.; Gentile, P.; Bidan, G.; Hadji, E.; Brousse, T.; Sadki, S., Highly Doped Silicon Nanowires Based Electrodes for Micro-Electrochemical Capacitor Applications. *Electrochem. Comm.* **2012**, *25*, 109-111.

76.   Thissandier, F.; Gentile, P.; Brousse, T.; Bidan, G.; Sadki, S., Are Tomorrow's Micro-Supercapacitors Hidden in a Forest of Silicon Nanotrees? *J. Power Sources* **2014**, *269*, 740-746.

77.   Gao, F.; Lewes-Malandrakis, G.; Wolfer, M. T.; Müller-Sebert, W.; Gentile, P.; Aradilla, D.; Schubert, T.; Nebel, C. E., Diamond-Coated Silicon Wires for Supercapacitor Applications in Ionic Liquids. *Diamond Relat. Mater.* **2015**, *51*, 1-6.

78.   Gao, F.; Wolfer, M. T.; Nebel, C. E., Highly Porous Diamond Foam as a Thin-Film Micro-Supercapacitor Material. *Carbon* **2014**, *80*, 833-840.

79.   Gao, F.; Nebel, C. E., Diamond-Based Supercapacitors: Realization and Properties. *ACS Appl. Mater.Interfaces* **2016**, *8*, 28244-28254.

80.   Barsoukov, E.; Macdonald, J. R., *Impedance Spectroscopy: Theory, Experiment, and Applications*; John Wiley & Sons, 2018.

81.   Wang, Y.; Guo, C. X.; Liu, J.; Chen, T.; Yang, H.; Li, C. M., Ceo2 Nanoparticles/Graphene Nanocomposite-Based High Performance Supercapacitor. *Dalton Trans.* **2011**, *40*, 6388-6391.

82.   Bhattacharya, G., et al., Probing the Flat Band Potential and Effective Electronic Carrier Density in Vertically Aligned Nitrogen Doped Diamond Nanorods Via Electrochemical Method. *Electrochim. Acta* **2017**, *246*, 68-74.

83.   Choe, H.-B.; Lee, H.-S.; Ismail, M. A.; Hussin, M. W., Evaluation of Electrochemical ımpedance Properties of Anticorrosionfilms by Arc Thermal Metal Spraying Method. *Int. J. Electrochem. Sci.* **2015**, *10*, 9775-9789.

84.   Dubal, D. P.; Lee, S. H.; Kim, J. G.; Kim, W. B.; Lokhande, C. D., Porous Polypyrrole Clusters Prepared by Electropolymerization for a High Performance Supercapacitor. *J. Mater. Chem.* **2012**, *22*, 3044-3052.

85.   Wei, N.; Jiang, Y.; Ying, Y.; Guo, X.; Wu, Y.; Wen, Y.; Yang, H., Facile Construction of a Polydopamine-Based Hydrophobic Surface for Protection of Metals against Corrosion. *RSC Adv.* **2017**, *7*, 11528-11536.

TOC Graphic